
PGOT: A Physics-Geometry Operator Transformer for Complex PDEs

Zhuo Zhang¹ Xi Yang¹ Ying Miao² Xiaobin Hu³ Yifu Gao¹
 Yuan Zhao¹ Yong Yang⁴ Canqun Yang⁵ Boocheong Khoo³

Abstract

While Transformers have demonstrated remarkable potential in modeling Partial Differential Equations (PDEs), modeling large-scale unstructured meshes with complex geometries remains a significant challenge. Existing efficient architectures often employ feature dimensionality reduction strategies, which inadvertently induces Geometric Aliasing, resulting in the loss of critical physical boundary information. To address this, we propose the Physics-Geometry Operator Transformer (PGOT), designed to reconstruct physical feature learning through explicit geometry awareness. Specifically, we propose Spectrum-Preserving Geometric Attention (SpecGeo-Attention). Utilizing a “physics slicing-geometry injection” mechanism, this module incorporates multi-scale geometric encodings to explicitly preserve multi-scale geometric features while maintaining linear computational complexity $O(N)$. Furthermore, PGOT dynamically routes computations to low-order linear paths for smooth regions and high-order non-linear paths for shock waves and discontinuities based on spatial coordinates, enabling spatially adaptive and high-precision physical field modeling. PGOT achieves consistent state-of-the-art performance across four standard benchmarks and excels in large-scale industrial tasks including airfoil and car designs.

1. Introduction

Partial Differential Equations (PDEs), derived from fundamental principles such as conservation of mass and energy, are ubiquitous in modeling complex phenomena across science and engineering, including fluid dynamics, structural

mechanics, and climate modeling (Cao et al., 2025). Traditional numerical methods, such as the Finite Element Method (FEM) (Zienkiewicz & Taylor, 2005) and Finite Volume Method (FVM) (Eymard et al., 2000), approximate solutions by discretizing PDEs onto meshes (Chen et al., 2025; Zhang et al., 2024). However, their reliance on dense mesh discretization imposes a heavy computational burden, often requiring much time and effort for multi-physics problems necessitating fine spatiotemporal resolution. Recently, Neural PDE Solvers have emerged as a promising paradigm, capable of learning resolution-invariant solution mappings between infinite-dimensional function spaces (Wang et al., 2025a; Li et al., 2025). By training on offline data, these operators can predict families of solutions under varying parameters orders of magnitude faster than traditional solvers, offering a promising direction for real-time scientific computing. Early spectral-based neural operators, such as the Fourier Neural Operator (FNO) (Li et al., 2021), rely on the fast Fourier transform. While they possess the remarkable ability to learn resolution-independent operators, they are inherently limited to regular grids, restricting their applicability to complex geometries and unstructured meshes. To address this, graph-based neural operators (Hao et al., 2023; Li et al., 2023b) treat input and output functions as graphs, employing message-passing mechanisms to generalize across different domain geometries. However, graph methods are often constrained by local receptive fields, making it difficult to effectively capture global long-range dependencies and suffer from low efficiency on large-scale nodes.

This necessitates the adoption of Transformers (Vaswani et al., 2017). The self-attention mechanism in Transformers is mathematically analogous to learning a global Green’s function (Cao, 2021), making it ideally suited for modeling non-local physical interactions (Alkin et al., 2024; Koshizuka et al., 2024). However, a fundamental scalability barrier remains: the standard self-attention mechanism exhibits quadratic computational complexity $\mathcal{O}(N^2)$ with respect to the number of mesh points N . Given that scientific simulations typically involve 10^5 to 10^7 grid points, standard Transformers are computationally intractable for high-resolution physics. Consequently, the research frontier has shifted towards efficient linear transformers (Li

¹National University of Defense Technology ²Peking University ³National University of Singapore ⁴Tiangong University ⁵National SuperComputer Center in Tianjin. Correspondence to: Xi Yang <yangxi1016@nudt.edu.cn>, Xiaobin Hu <ben0xiaobin0hu1@nus.edu.sg>.

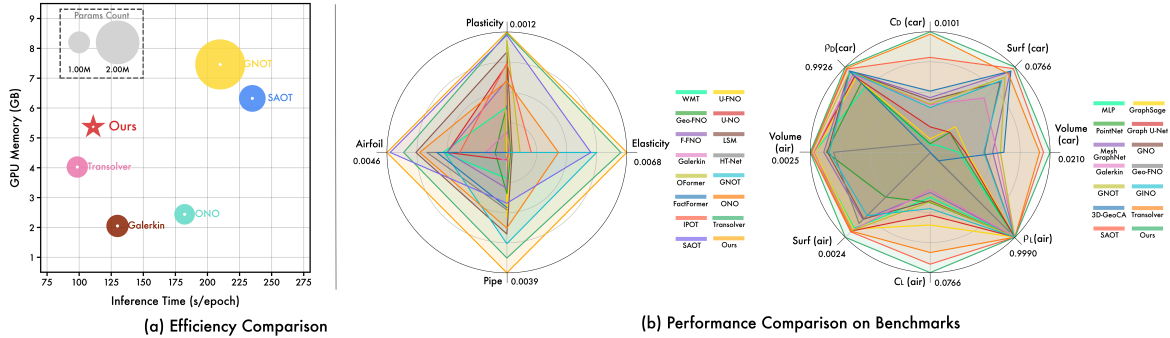


Figure 1. Efficiency and accuracy comparison on standard benchmarks. (a) Inference speed vs. Memory usage. Bubble size indicates model size. (b) Multi-dimensional performance metrics on PDE and industrial datasets.

et al., 2023c; Luo et al., 2025; Wu et al., 2024). Recent state-of-the-art methods employ strategies such as low-rank approximations or token clustering to reduce the effective sequence length, achieving linear complexity $\mathcal{O}(N)$ (Rao et al., 2021; Xiao et al., 2024). While these architectures successfully improve throughput, they often do so at the cost of geometric and physical fidelity, as follows:

L1): Aggregating local mesh points into latent tokens implicitly acts as a spatial low-pass filter, causing geometric aliasing where high-frequency boundary details are erased.

L2): Allocating a uniform computational budget across the domain neglects physical heterogeneity, resulting in over-smoothed shocks in discontinuity regions and redundant computations in smooth flows.

To bridge the gap between computational efficiency and high-fidelity physical modeling, we present the Physics-Geometry Operator Transformer (PGOT). Unlike prior methods that treat geometry merely as a supplementary input, PGOT intertwines physical state aggregation with explicit geometric reconstruction. Specifically, PGOT first projects physical fields into compact latent slices, while explicitly injecting multi-scale geometric embeddings during the reconstruction phase. This eliminates geometric aliasing caused by conventional dimensionality reduction while maintaining $\mathcal{O}(N)$ linear complexity (**Solving L1**). Subsequently, the model dynamically routes computational paths based on local flow complexity. This design ensures the model is both spectrum-preserving to avoid aliasing and spatially adaptive to handle physical heterogeneity (**Solving L2**). Extensive experiments demonstrate that PGOT achieves state-of-the-art performance on standard benchmarks and industrial applications, as illustrated by the efficiency-accuracy trade-off in Figure 1.

Our main contributions are as follows:

- Our proposed PGOT framework addresses the geometric aliasing bottleneck inherent in complex mesh

modeling, thereby reconciling computational efficiency with physical fidelity.

- We propose the SpecGeo-Attention mechanism to decouple global physical aggregation from local geometric reconstruction via a “physics slicing-geometry injection” paradigm, thereby preserving complex boundary features with high fidelity.
- By dynamically routing computations to linear or non-linear paths based on flow heterogeneity, the Taylor-decomposed Feed-Forward Network efficiently captures multi-scale physical features while enhancing model interpretability.

2. Related Work

2.1. Physics-Informed Neural Networks

Physics-Informed Neural Networks (PINNs) (Raissi et al., 2019) represent a foundational paradigm for solving PDEs by embedding governing equations directly into the loss function. PINNs parameterize the solution as a neural network and minimize the PDE residual at collocation points, enabling mesh-free training without labeled simulation data. However, PINNs face fundamental limitations for the problems we target. First, PINNs solve individual PDE instances, requiring complete retraining for each new parameter configuration or boundary condition—a prohibitive cost for design optimization requiring thousands of evaluations. Second, for complex geometries and multi-physics coupling, PINNs frequently encounter ill-conditioning issues (Zhang et al., 2025b;a), often leading to convergence failures or accuracy degradation. Although recent research has alleviated these problems through parameterization (Cho et al., 2024), meta-learning (Cheng & Alkhalifah, 2025), and transfer learning (Wang et al., 2025b) strategies, PINNs still struggle to maintain accuracy and efficiency when the configuration space becomes sufficiently large. These limitations motivate the development of the neural operator paradigm.

2.2. Neural Operators for PDEs

Neural operators have emerged as a powerful paradigm for learning resolution-invariant mappings between infinite-dimensional function spaces (Kovachki et al., 2023). DeepONet (Lu et al., 2021) pioneered this field by approximating operators through a Branch-Trunk architecture. Subsequently, the Fourier Neural Operator (FNO) (Li et al., 2021) established new benchmarks by parameterizing the integral kernel directly in the frequency domain using FFT. To address the limitations of standard FNO, numerous variants have been proposed: U-NO (Rahman et al., 2023) and U-FNO (Wen et al., 2022) integrate U-Net structures to capture multi-scale features, while F-FNO (Tran et al., 2023) improves computational efficiency by factorizing the Fourier representation across dimensions. To handle irregular geometries beyond rectangular grids, Geo-FNO (Li et al., 2023a) maps physical domains to latent uniform grids, while LSM (Wu et al., 2023) and LNO (Wang & Wang, 2024) apply spectral methods within learned low-dimensional latent spaces to tackle high-dimensional PDE problems. Furthermore, to mitigate the global nature of Fourier transforms that typically leads to loss of local details, wavelet-based methods such as WMT (Gupta et al., 2021) and WNO (Tripura & Chakraborty, 2023) have been introduced to leverage the time-frequency localization properties of wavelets for capturing local variations. For modeling complex unstructured meshes, geometric deep learning offers an alternative perspective. Graph Neural Operators (GNO) (Li et al., 2020) and MeshGraphNet (Pfaff et al., 2021) treat physical domains as graphs, employing message-passing mechanisms to handle complex boundaries. To combine global spectral processing capabilities with local geometric flexibility, hybrid architectures have emerged. For instance, GINO (Li et al., 2023b) integrates Geo-FNO’s global spectral capabilities with GNO’s local graph processing, while 3D-GeoCA (Deng et al., 2024) further incorporates pre-trained 3D vision backbones to enhance geometric feature extraction. However, graph-based methods typically suffer from geometric instability (Morris et al., 2023; Luo et al., 2025) and incur high computational overhead when scaling to million-scale mesh points due to neighborhood search and message passing.

2.3. Transformers for PDEs

The Transformer architecture has garnered significant attention in scientific computing due to its global receptive field and superior modeling capabilities. Early works such as OFormer (Li et al., 2023c) and HT-Net (Liu et al., 2024) demonstrated the potential of attention mechanisms in capturing non-local physical interactions. However, the quadratic complexity $\mathcal{O}(N^2)$ of standard attention remains a bottleneck restricting its scalability. To achieve linear complexity $\mathcal{O}(N)$, recent research has explored diverse path-

ways: AFNO (Guibas et al., 2022), FNet (Lee-Thorp et al., 2022), and GFNet (Rao et al., 2021) attempt token mixing in the Fourier domain, while SAOT (Zhou et al., 2025) further integrates wavelet attention to mitigate aliasing issues; simultaneously, Galerkin Transformer (Cao, 2021), GNOT (Hao et al., 2023), and ONO (Xiao et al., 2024) utilize kernel tricks or low-rank approximations to achieve linearization; whereas methods represented by FactFormer (Li et al., 2023d) and Transolver (Wu et al., 2024) employ axial decomposition or token aggregation strategies, respectively. Despite their significant efficiency improvements, these dimensionality reduction or aggregation operations act as implicit spatial low-pass filters, inevitably discarding high-frequency geometric details. Furthermore, they typically allocate a uniform computational budget across the entire domain, failing to adapt to physical heterogeneity in flow fields.

3. Method

In this section, we present the design of the Physics-Geometry Operator Transformer (PGOT). We first analyze the geometric aliasing bottleneck inherent in existing efficient architectures. Subsequently, we detail the two core components: Spectrum-Preserving Geometric Attention (SpecGeo-Attention) and the Taylor-Decomposed Feed-Forward Network (TaylorDecomp-FFN). The overall architecture is illustrated in Figure 2.

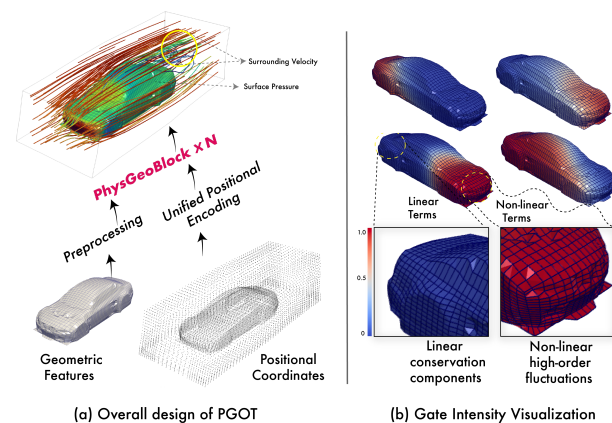


Figure 2. Overall architecture of PGOT. (a) The framework explicitly integrates multi-scale geometry via stacked PhysGeoBlocks to reconstruct velocity and pressure fields on complex 3D meshes. (b) Visualization of TaylorDecomp-FFN. The Linear Expert (blue) captures smooth conservation dynamics, while the Non-linear Expert (red) targets high-order fluctuations.

3.1. Problem Formulation

We consider a physical system governed by partial differential equations (PDEs), where the solution operator \mathcal{G}^\dagger

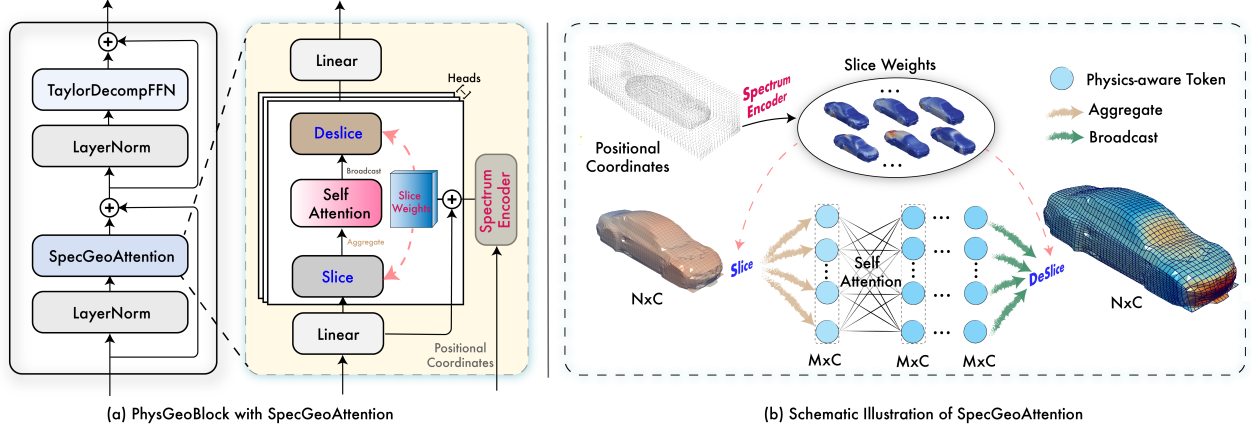


Figure 3. Architecture of PhysGeoBlock and SpecGeo-Attention. (a) The PhysGeoBlock integrates explicit geometric coordinates into the SpecGeo-Attention and TaylorDecomp-FFN layers. (b) The “physics slicing-geometry injection” paradigm. A Spectrum Encoder generates geometry-aware weights to aggregate N mesh points into M latent tokens (Slice) and reconstruct them (DeSlice). This design achieves linear complexity $\mathcal{O}(N)$ while preserving multi-scale geometric fidelity.

maps an input function space to an output function space: $\mathcal{G}^\dagger : \mathcal{A}(\Omega; \mathbb{R}^{d_a}) \rightarrow \mathcal{U}(\Omega; \mathbb{R}^{d_u})$. In practice, the continuous domain $\Omega \subset \mathbb{R}^d$ is discretized into N mesh points $\mathbf{G} = \{\mathbf{g}_i\}_{i=1}^N$. The input and output functions are sampled as $\mathbf{a} \in \mathbb{R}^{N \times d_a}$ and $\mathbf{u} \in \mathbb{R}^{N \times d_u}$, respectively. Our goal is to learn a parameterized neural operator \mathcal{G}_θ that approximates the ground truth operator \mathcal{G}^\dagger .

Existing efficient Transformers achieve linear complexity through feature aggregation. However, this operation acts as a low-pass filter in the frequency domain. Let $f(\mathbf{g})$ be the geometric signal. Aggregation can be modeled as a convolution with a smoothing kernel K_σ . According to the convolution theorem, the frequency response is $\hat{f}_{agg}(\omega) = \hat{K}_\sigma(\omega) \cdot \hat{f}(\omega)$. When the spatial frequency $|\omega|$ exceeds the cutoff frequency $\omega_c \propto 1/\sigma$, $\hat{K}_\sigma(\omega) \approx 0$, causing high-frequency geometric details to be irreversibly erased. We term this phenomenon geometric aliasing, identifying it as a fundamental bottleneck limiting performance on complex boundaries. PGOT addresses this via explicit multi-scale geometric reconstruction.

3.2. PGOT

Recent work has demonstrated that slice-based attention, which aggregates mesh points into learnable physics-aware tokens, can achieve linear complexity for PDE solving (Wu et al., 2024). However, this aggregation implicitly acts as a spatial low-pass filter, causing geometric aliasing at complex boundaries. To address this limitation, PGOT introduces Spectrum-Preserving Geometric Attention and Taylor-Decomposed Feed-Forward Networks.

$$\mathbf{X}^0 = \mathcal{P}_\theta(\mathbf{a} \oplus \mathcal{E}_{\text{pos}}(\mathbf{G})), \quad (1)$$

where \oplus denotes concatenation, and \mathcal{P}_θ is a lifting MLP. We employ a Unified Reference Point Encoding \mathcal{E}_{pos} to ensure discretization invariance.

The processor consists of L stacked *PhysGeoBlocks*, as depicted in Figure 3(a). Unlike prior methods that use coordinates only at the input, PGOT explicitly injects geometry \mathbf{G} at every layer:

$$\hat{\mathbf{X}}^l = \mathbf{X}^{l-1} + \text{SpecGeo-Attn}(\text{LN}(\mathbf{X}^{l-1}); \mathbf{G}), \quad (2)$$

$$\mathbf{X}^l = \hat{\mathbf{X}}^l + \text{TaylorDecomp}(\text{LN}(\hat{\mathbf{X}}^l); \mathbf{G}), \quad (3)$$

where $\text{LN}(\cdot)$ denotes Layer Normalization. This design ensures that geometric guidance persists throughout the deep network evolution.

3.2.1. SPECTRUM-PRESERVING GEOMETRIC ATTENTION

As illustrated in Figure 3(b), the core philosophy of SpecGeo-Attention is to decouple global physical state aggregation from local geometric reconstruction.

Multi-Scale Geometric Spectral Encoding. To reconstruct high-frequency information lost during aggregation, we inject multi-scale geometric encodings prior to slicing. We design a bank of encoders for S scales:

$$\mathbf{h}_s = \phi_s(10^{s-1} \cdot \mathbf{g}), \quad s = 1, \dots, S, \quad (4)$$

where ϕ_s is a two-layer MLP. The exponential scaling factor 10^{s-1} ensures coverage of diverse spatial frequencies: $s = 1$ captures macro-structures, while higher scales capture micro-boundary details. These features are fused via

concatenation to preserve full spectral information:

$$\Phi_{\text{geo}}(\mathbf{g}) = \sigma_{\text{act}}(\mathbf{W}_{\text{fuse}} \cdot [\mathbf{h}_1; \mathbf{h}_2; \dots; \mathbf{h}_S]), \quad (5)$$

where $[\cdot; \cdot]$ denotes concatenation.

Geometry-Informed Physics Slicing. The geometric encoding is injected into the physical features to guide the slicing process:

$$\tilde{\mathbf{X}}_q = \mathbf{X}\mathbf{W}_x + \Phi_{\text{geo}}(\mathbf{G}). \quad (6)$$

We then compute the soft assignment matrix $\mathbf{A} \in \mathbb{R}^{N \times M}$ mapping N mesh points to M latent physical states:

$$\mathbf{A}_{ij} = \frac{\exp([\tilde{\mathbf{X}}_q]_i \cdot \mathbf{w}_j / \tau)}{\sum_{k=1}^M \exp([\tilde{\mathbf{X}}_q]_i \cdot \mathbf{w}_k / \tau)}, \quad (7)$$

where $\{\mathbf{w}_j\}$ are learnable slice prototypes. Since \mathbf{A} is derived from geometry-enhanced features, the clustering respects complex boundaries (e.g., distinguishing the pressure side from the suction side of an airfoil).

Physical features are then aggregated into latent tokens $\mathbf{Z} \in \mathbb{R}^{M \times C}$ via $\mathbf{Z} = \mathbf{D}^{-1} \mathbf{A}^\top (\mathbf{X}\mathbf{W}_f)$, processed by standard Multi-Head Self-Attention (MHSA), and reconstructed back to the mesh domain:

$$\mathbf{X}' = \mathbf{A} \cdot \text{MHSA}(\mathbf{Z}). \quad (8)$$

This entire process maintains $\mathcal{O}(N)$ complexity while preserving geometric fidelity.

3.2.2. TAYLORDECOMP-FFN

Physical fields exhibit significant spatial heterogeneity: smooth laminar regions follow low-order linear laws, while shocks and discontinuities are governed by high-order non-linear dynamics. Drawing inspiration from Taylor series expansion, we approximate the solution operator at any spatial point \mathbf{g} by decomposing it into low-order and high-order components:

$$\mathbf{u}(\mathbf{g}) \approx \underbrace{\mathbf{u}(\mathbf{g}_0) + \nabla \mathbf{u}|_{\mathbf{g}_0}(\mathbf{g} - \mathbf{g}_0)}_{\text{Linear Terms}} + \underbrace{\mathcal{R}_{\text{high}}(\mathbf{g})}_{\text{Non-linear Residuals}}. \quad (9)$$

To adaptively model these terms, we propose the TaylorDecomp-FFN, which formulates the feature transformation as a dynamic composition of two expert paths:

$$\mathbf{X}_{\text{out}} = (\mathbf{1} - \alpha(\mathbf{g})) \odot \mathcal{F}_{\text{lin}}(\mathbf{X}) + \alpha(\mathbf{g}) \odot \mathcal{F}_{\text{non}}(\mathbf{X}). \quad (10)$$

The architecture explicitly instantiates the theoretical decomposition above. The Linear Expert (\mathcal{F}_{lin}), corresponding to the low-order Taylor terms, consists of a streamlined linear projection with dropout to efficiently capture smooth conservation dynamics:

$$\mathcal{F}_{\text{lin}}(\mathbf{x}) = \mathbf{W}_{l2}(\text{Dropout}(\mathbf{W}_{l1}\mathbf{x})). \quad (11)$$

In parallel, the Non-linear Expert (\mathcal{F}_{non}) targets the high-order residuals, utilizing a deeper MLP with activation functions to resolve sharp gradients and discontinuities:

$$\mathcal{F}_{\text{non}}(\mathbf{x}) = \mathbf{W}_{n2}(\sigma(\mathbf{W}_{n1}\mathbf{x})). \quad (12)$$

The dynamic routing between these paths is governed by a spatial gate $\alpha(\mathbf{g}) \in [0, 1]^C$, which is generated via an Absolute Coordinate Embedding (ACE):

$$\alpha(\mathbf{g}) = \text{Sigmoid}(\text{MLP}_{\text{gate}}(\text{PosEmbed}(\mathbf{g}))). \quad (13)$$

We employ *unconstrained regime selection* where the gate α operates independently per channel. This flexibility allows the model to fully activate the non-linear path in shock regions ($\alpha \rightarrow 1$), rely on the linear path in smooth flows ($\alpha \rightarrow 0$), or leverage a hybrid combination ($\alpha \approx 0.5$) in complex transition zones.

4. Experiments

We evaluate PGOT on four standard benchmarks and two large-scale industrial simulations, covering diverse geometric settings from point clouds to complex 3D unstructured meshes.

4.1. Experimental Setup

Datasets. Our evaluation encompasses six benchmarks with varying geometric complexities. The standard benchmarks (Li et al., 2021; 2023a) include Elasticity (inner stress prediction on 2D point clouds), Plasticity (temporal displacement forecasting under external forces), Airfoil (transonic flow simulation with shock waves), and Pipe (velocity field estimation in curved structures). For industrial-scale validation, we employ Shape-Net Car (Umetani & Bickel, 2018) for automotive aerodynamic simulation on hybrid 3D geometries, and AirFRANS (Bonnet et al., 2022) for high-fidelity RANS simulation on NACA airfoils under varying Reynolds numbers and angles of attack. Detailed dataset descriptions are provided in Appendix A.1.

Baselines. We compare against representative methods from three categories: spectral neural operators (FNO (Li et al., 2021), Geo-FNO (Li et al., 2023a), U-NO (Rahman et al., 2023), F-FNO (Tran et al., 2023), LSM (Wu et al., 2023), WMT (Gupta et al., 2021)); Transformer-based approaches (Galerkin Transformer (Cao, 2021), OFormer (Li et al., 2023c), GNOT (Hao et al., 2023), ONO (Xiao et al., 2024), FactFormer (Li et al., 2023d), IPOT (Lee & Oh, 2024), Transolver (Wu et al., 2024), SAOT (Zhou et al., 2025)); and geometric deep learning methods (PointNet (Qi et al., 2017), Graph U-Net (Gao & Ji, 2019), GraphSAGE (Hamilton et al., 2017), MeshGraphNet (Pfaff et al., 2021), GNO (Li et al., 2020), GINO (Li et al., 2023b), 3D-GeoCA (Deng et al., 2024)). See Appendix A.4 for details.

Metrics and Implementation. We adopt the relative L^2 error as the primary evaluation metric. For industrial benchmarks, we additionally report aerodynamic coefficient errors and Spearman’s rank correlation. PGOT is configured with $L = 8$ PhysGeoBlocks, with other hyperparameters adapted to each task. All experiments are conducted on NVIDIA A100 GPUs and repeated three times. Comprehensive details on metrics, training configurations, and hyperparameters are provided in [Appendix A.2](#) and [Appendix A.3](#).

4.2. Main Results

Table 1. Performance comparison on standard benchmarks. The relative L^2 error is reported. The best results are highlighted in **bold**, and the second best are underlined. Gray background indicates our proposed method. Improvement denotes the reduction in relative error.

Model	Structured Mesh			Point Cloud
	Plasticity	Pipe	Airfoil	Elasticity
WMT (2021)	0.0076	0.0077	0.0075	0.0359
U-FNO (2022)	0.0039	0.0056	0.0269	0.0239
Geo-FNO (2023a)	0.0074	0.0067	0.0138	0.0229
U-NO (2023)	0.0034	0.0100	0.0078	0.0258
F-FNO (2023)	0.0047	0.0070	0.0078	0.0263
LSM (2023)	0.0025	0.0050	0.0059	0.0218
Galerkin (2021)	0.0120	0.0098	0.0118	0.0240
HT-Net (2024)	0.0333	0.0059	0.0065	/
OFormer (2023c)	0.0017	0.0168	0.0183	0.0183
GNOT (2023)	0.0336	0.0047	0.0076	0.0086
FactFormer (2023d)	0.0312	0.0060	0.0071	/
ONO (2024)	0.0048	0.0052	0.0061	0.0118
IPOT (2024)	0.0033	/	0.0088	0.0156
Transolver (2024)	<u>0.0013</u>	<u>0.0043</u>	0.0053	<u>0.0079</u>
SAOT (2025)	0.0014	0.0062	<u>0.0051</u>	0.0090
PGOT (Ours)	0.0012	0.0039	0.0046	0.0069
Improvement	7.7%	9.3%	9.8%	12.7%

Standard Benchmarks. Table 1 presents the performance comparison on four standard benchmarks. PGOT consistently achieves state-of-the-art results across all datasets, with relative error reductions ranging from 7.7% to 12.7% compared to the second-best methods. On Plasticity and Pipe, PGOT outperforms Transolver by 7.7% and 9.3%, respectively, demonstrating the effectiveness of explicit geometric injection in capturing temporal dynamics and curved boundary features. For Airfoil, where shock waves introduce sharp discontinuities, PGOT achieves 9.8% improvement over SAOT, validating the benefit of TaylorDecompFFN in adaptively routing computations to non-linear paths for discontinuity regions. This is qualitatively supported by Figure 4, where PGOT produces substantially cleaner predictions near shock waves compared to Transolver and SAOT. The most significant improvement (12.7%) is observed on Elasticity, a point cloud benchmark where geometric information is particularly sparse. As visualized in

Figure 4 (right), baselines exhibit scattered high-error points, whereas PGOT maintains consistently low errors, highlighting the importance of multi-scale geometric encoding in preserving structural details.

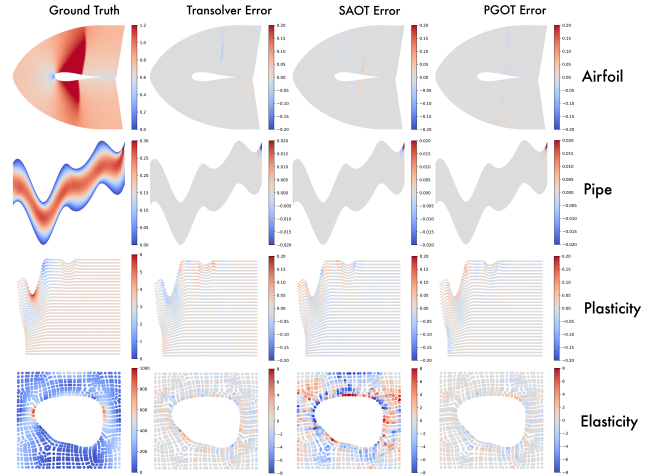


Figure 4. Visualization of prediction errors on standard benchmarks. The first column shows ground truth fields, and the remaining columns display prediction errors.

Industrial Simulations. Table 2 summarizes results on large-scale industrial benchmarks. On Shape-Net Car, PGOT achieves the best performance across all metrics, with 9.1% reduction in volumetric field error and 10.6% improvement in drag coefficient prediction compared to Transolver. The Spearman correlation $\rho_D = 0.9926$ indicates excellent ranking capability for design optimization. Figure 5(b) visualizes these results, showing excellent agreement between PGOT’s predicted streamlines and ground truth, with superior accuracy in geometrically complex regions like wheel wells. On AirFRANS, PGOT demonstrates substantial improvements: 32.4% reduction in volumetric field error, 81.3% reduction in surface field error, and 12.2% improvement in lift coefficient prediction. As shown in Figure 5(a), while Transolver and SAOT produce radial error patterns, PGOT achieves significantly cleaner predictions with errors primarily concentrated in the far-field region. These results underscore PGOT’s capability in handling complex unstructured meshes with over 32,000 points while maintaining high prediction fidelity. Efficiency analysis is detailed in [Appendix B.2](#).

4.3. Ablation Studies

We conduct systematic ablation studies to validate the contribution of each proposed component. We report results on four standard benchmarks (Plasticity, Pipe, Airfoil, Elasticity) in the main text to cover diverse geometric types and physical regimes; full results covering all datasets are provided in [Appendix B.1](#).

Table 2. Performance comparison on practical design tasks. For Shape-Net Car, relative L^2 of surrounding (Volume) and surface (Surf) physics fields is recorded. For AirfRANS, MSE of Volume and Surf fields is recorded. The relative L^2 of drag coefficient (C_D) and lift coefficient (C_L) is also recorded, along with their Spearman’s rank correlations ρ_D and ρ_L . A Spearman’s correlation close to 1 indicates better performance. “/” indicates the baseline cannot apply to this benchmark.

Model	Shape-Net Car				AirfRANS			
	Volume ↓	Surf ↓	C_D ↓	ρ_D ↑	Volume ↓	Surf ↓	C_L ↓	ρ_L ↑
Simple MLP	0.0512	0.1304	0.0307	0.9496	0.0081	0.0200	0.2108	0.9932
GraphSAGE (2017)	0.0461	0.1050	0.0270	0.9695	0.0087	0.0184	0.1476	0.9964
PointNet (2017)	0.0494	0.1104	0.0298	0.9583	0.0253	0.0996	0.1973	0.9919
Graph U-Net (2019)	0.0471	0.1102	0.0226	0.9725	0.0076	0.0144	0.1677	0.9949
MeshGraphNet (2021)	0.0354	0.0781	0.0168	0.9840	0.0214	0.0387	0.2252	0.9945
GNO (2020)	0.0383	0.0815	0.0172	0.9834	0.0269	0.0405	0.2016	0.9938
Galerkin (2021)	0.0339	0.0878	0.0179	0.9764	0.0074	0.0159	0.2336	0.9951
Geo-FNO (2023a)	0.1670	0.2378	0.0664	0.8280	0.0361	0.0301	0.6161	0.9257
GNOT (2023)	0.0329	0.0798	0.0178	0.9833	0.0049	0.0152	0.1992	0.9942
GINO (2023b)	0.0386	0.0810	0.0184	0.9826	0.0297	0.0482	0.1821	0.9958
3D-GeoCA (2024)	0.0319	0.0779	0.0159	0.9842	/	/	/	/
Transolver (2024)	<u>0.0231</u>	<u>0.0787</u>	<u>0.0113</u>	<u>0.9901</u>	<u>0.0037</u>	0.0142	0.1030	0.9978
SAOT (2025)	<u>0.0223</u>	<u>0.0778</u>	0.0122	0.9884	0.0038	<u>0.0128</u>	<u>0.0872</u>	<u>0.9983</u>
PGOT (Ours)	0.0210	0.0766	0.0101	0.9926	0.0025	0.0024	0.0766	0.9990
Improvement	9.1%	1.5%	10.6%	/	32.4%	81.3%	12.2%	/

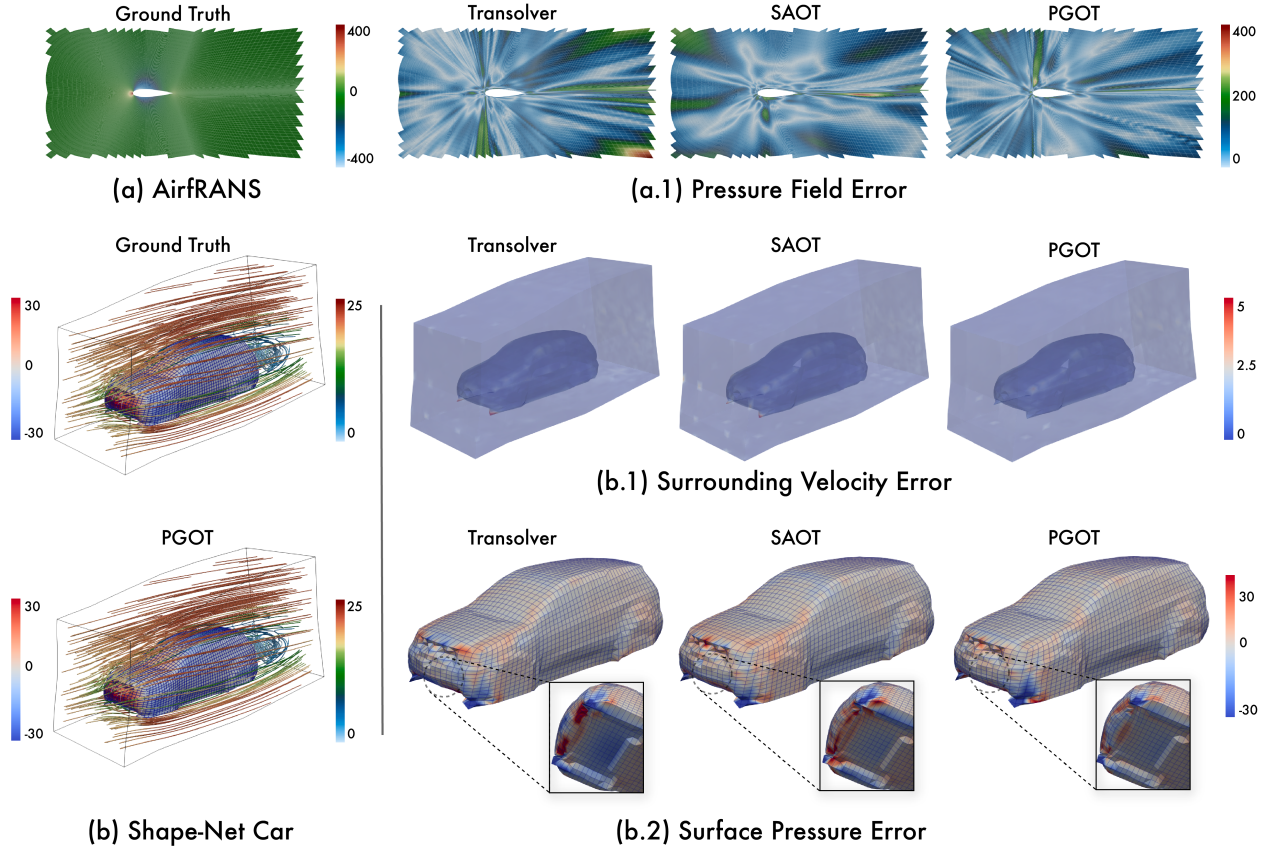


Figure 5. Visualization on industrial benchmarks. (a) AirfRANS: ground truth pressure field and prediction errors. (b) Shape-Net Car: ground truth streamlines and PGOT prediction, along with surrounding velocity and surface pressure errors.

Table 3. Ablation on the number of latent slices M . We observe that $M = 64$ offers the best trade-off for standard benchmarks.

Slices M	Plasticity	Pipe	Airfoil	Elasticity
8	0.0104	0.0079	0.0194	0.0239
16	0.0047	0.0071	0.0101	0.0074
32	0.0025	0.0040	0.0049	0.0081
64	0.0012	0.0039	0.0046	<u>0.0069</u>
128	0.0021	0.0051	0.0056	0.0061
256	0.0134	0.0044	0.0048	0.0079

Number of Latent Slices M . Table 3 examines the impact of varying M . Performance generally improves as M increases, with Plasticity, Pipe, and Airfoil peaking at $M = 64$. Interestingly, Elasticity benefits from even finer granularity, reaching its best performance at $M = 128$ (0.0061). This is likely because point cloud data lacks explicit connectivity, requiring more slices to capture local geometric nuances. However, further increasing M to 256 leads to degradation across all tasks due to the fragmentation of coherent physical regions. Considering the trade-off between accuracy and computational cost, we adopt $M = 64$ as the unified default.

Table 4. Ablation on the number of geometric scales S . Multi-scale encoding ($S = 2$) significantly outperforms single-scale baselines.

Scales S	Plasticity	Pipe	Airfoil	Elasticity
1	0.0104	0.0079	0.0194	0.0239
2	0.0012	0.0039	0.0046	0.0069
3	0.0047	0.0071	0.0101	0.0074
4	0.0021	0.0051	0.0056	0.0079

Number of Geometric Scales S . Table 4 investigates the effect of multi-scale geometric encoding. Single-scale encoding ($S = 1$) performs poorly across all benchmarks, confirming that aggregation-induced geometric aliasing significantly degrades prediction quality. Performance improves substantially and reaches optimality at $S = 2$, demonstrating that a dual-scale representation is sufficient to capture both global topology and local boundary details. Interestingly, further increasing the scales to $S = 3$ or $S = 4$ leads to performance degradation. This suggests that excessive high-frequency geometric priors may introduce spectral noise or redundancy, which interferes with the model’s ability to learn robust physical dynamics. See Appendix C for additional visualizations.

Component Analysis. Table 5 validates the necessity of both proposed modules. Removing SpecGeo-Attention (w/o SGA) leads to performance drops across all tasks, particularly in Elasticity (0.0069 \rightarrow 0.0074) and Airfoil

Table 5. Both SpecGeo-Attention (SGA) and TaylorDecomp-FFN (TDF) are critical for optimal performance.

Variant	Plasticity	Pipe	Airfoil	Elasticity
w/o SGA	0.0093	0.0045	0.0104	0.0074
w/o TDF	0.0134	0.0089	0.0094	0.0231
Full PGOT	0.0012	0.0039	0.0046	0.0069

(0.0046 \rightarrow 0.0104), confirming that explicit geometric injection is crucial for handling irregular point clouds and shock boundaries. Removing TaylorDecomp-FFN (w/o TDF) causes severe degradation in Plasticity (0.0012 \rightarrow 0.0134), validating the importance of adaptive routing for time-dependent heterogeneous fields.

4.4. Out-of-Distribution (OOD) Generalization

We evaluate PGOT on AirfRANS under two extrapolation settings: (1) Unseen Reynolds and (2) Unseen Angles. As shown in Table 6, PGOT demonstrates superior robustness against 11 baselines. In Reynolds extrapolation, PGOT achieves the lowest lift coefficient error ($C_L = 0.2942$) and the highest ranking correlation ($\rho_L = 0.9923$). In Angle extrapolation, PGOT maintains the highest ranking consistency ($\rho_L = 0.9952$), significantly outperforming graph-based methods and surpassing the SOTA Transolver. This confirms that explicitly modeling geometry-physics interactions enables robust reasoning in unseen physical regimes. Detailed analysis are provided in Appendix B.3.

Table 6. OOD generalization on AirfRANS.

Model	Unseen Reynolds		Unseen Angles	
	$C_L \downarrow$	$\rho_L \uparrow$	$C_L \downarrow$	$\rho_L \uparrow$
Simple MLP	0.6205	0.9578	0.4128	0.9572
GraphSAGE (2017)	0.4333	0.9707	0.2538	0.9894
PointNet (2017)	0.3836	0.9806	0.4425	0.9784
Graph U-Net (2019)	0.4664	0.9645	0.3756	0.9816
MeshGraphNet (2021)	1.7718	0.7631	0.6525	0.8927
GNO (2020)	0.4408	0.9878	0.3038	0.9884
Galerkin (2021)	0.4615	0.9826	0.3814	0.9821
GNOT (2023)	0.3268	0.9865	0.3497	0.9868
GINO (2023b)	0.4180	0.9645	0.2583	0.9923
Transolver (2024)	<u>0.3042</u>	<u>0.9899</u>	0.1503	<u>0.9948</u>
SAOT (2025)	0.4242	0.9764	0.2925	0.9888
PGOT (Ours)	0.2942	0.9923	<u>0.1742</u>	0.9952

5. Conclusion

In this work, we proposed PGOT to address the geometric aliasing bottleneck in efficient neural operators. By synergizing Spectrum-Preserving Geometric Attention with a regime-adaptive Taylor-Decomposed FFN, our framework reconciles linear complexity with high-fidelity boundary

reconstruction. PGOT achieves state-of-the-art results on industrial benchmarks and demonstrates superior robustness in extrapolation tasks. Future avenues include extending this geometric-physical decoupling paradigm to multi-physics foundation models.

Appendix A. Implementation Details

Appendix A.1. Dataset Descriptions

We provide detailed descriptions of all six benchmarks used in our evaluation. Table 7 summarizes the key statistics.

Table 7. Summary of benchmark datasets. #Mesh denotes the number of discretized mesh points per sample.

Geometry	Benchmark	Dim	#Mesh	Input	Output	Train / Test
Point Cloud	Elasticity	2D	972	Structure	Inner Stress	1000 / 200
	Plasticity	2D+T	3,131	External Force	Displacement	900 / 80
Structured Mesh	Airfoil	2D	11,271	Structure	Mach Number	1000 / 200
	Pipe	2D	16,641	Structure	Velocity	1000 / 200
Unstructured Mesh	Shape-Net Car	3D	32,186	Structure	Velocity, Pressure	789 / 100
	AirFRANS	2D	32,000	Structure	Velocity, Pressure	800 / 200

Elasticity. This benchmark involves predicting the inner stress distribution of elastic materials based on geometric structures, discretized as 972 scattered points in 2D space. Each sample represents a different material structure, and the model must estimate the stress tensor at each point. The training set contains 1000 samples, and the test set contains 200 samples (Li et al., 2021; Wu et al., 2024).

Plasticity. The task is to predict future deformations of plastic materials under impact from arbitrarily-shaped dies. The input consists of structured meshes with 101×31 points representing the die geometry, and the output is the displacement field over 20 future time steps containing four directional deformation components. The training set contains 900 samples, and the test set contains 80 samples (Li et al., 2021; Wu et al., 2024).

Airfoil. This benchmark requires estimating Mach number distributions around airfoil geometries on structured meshes with 221×51 points. All shapes are deformations of the NACA-0012 baseline airfoil. The task involves transonic flow regimes where shock waves introduce discontinuities in the solution field. The training set contains 1000 samples, and the test set contains 200 samples (Li et al., 2021; Wu et al., 2024).

Pipe. The objective is to predict horizontal fluid velocity fields based on curved pipe structures. Each sample is discretized into a 129×129 structured mesh, with different samples generated by varying the pipe centerline geometry. The training set contains 1000 samples, and the test set contains 200 samples (Li et al., 2021; Wu et al., 2024).

Shape-Net Car. This industrial benchmark focuses on automotive aerodynamic simulation at 72 km/h driving conditions. The task requires simultaneous prediction of surface pressure and surrounding air velocity. Vehicle geometries are sourced from the “car” category of the ShapeNet repository and discretized into unstructured meshes with approximately 32,000 points combining surface and volumetric elements. The input is preprocessed to include mesh point positions, signed distance functions, and normal vectors. The predicted fields can be used to compute drag coefficients for design optimization. The training set contains 789 samples, and the test set contains 100 samples (Umetani & Bickel, 2018).

AirFRANS. This dataset contains high-fidelity Reynolds-Averaged Navier-Stokes simulation data for airfoils from the NACA 4- and 5-digit series. Unlike the Airfoil benchmark, AirFRANS features diverse airfoil shapes under varying Reynolds numbers (3×10^6 to 6×10^6) and angles of attack (-5 to 15), with finer unstructured meshes of 32,000 points per sample. Air velocity, pressure, and viscosity are recorded for surrounding regions, along with surface pressure. Both lift and drag coefficients can be computed from the predicted fields. However, as noted in the original paper, air velocity estimation remains challenging for aircraft, causing all deep models to perform poorly on drag coefficient prediction. Therefore, we focus primarily on lift coefficient and volume/surface physical quantity prediction accuracy. The training set contains 800 samples, and the test set contains 200 samples (Bonnet et al., 2022).

Appendix A.2. Evaluation Metrics

Relative L^2 Error. Given the ground-truth physical field \mathbf{u} and the model prediction $\hat{\mathbf{u}}$, the relative L^2 error is defined as:

$$\text{Relative } L^2 = \frac{\|\mathbf{u} - \hat{\mathbf{u}}\|_2}{\|\mathbf{u}\|_2}. \quad (14)$$

This metric is used across all benchmarks to measure the accuracy of predicted physical fields.

Aerodynamic Coefficient Error. For Shape-Net Car and AirFRANS, we compute aerodynamic coefficients from the predicted fields and report their relative errors. For unit density fluid, the coefficient (drag or lift) is defined as:

$$C = \frac{2}{v^2 A} \left[\int_{\partial\Omega} p(\xi) (\hat{\mathbf{n}}(\xi) \cdot \hat{\mathbf{i}}(\xi)) d\xi + \int_{\partial\Omega} \tau(\xi) \cdot \hat{\mathbf{i}}(\xi) d\xi \right], \quad (15)$$

where v is the inlet flow speed, A is the reference area, $\partial\Omega$ denotes the object surface, p is the pressure function, $\hat{\mathbf{n}}$ is the outward unit normal vector of the surface, $\hat{\mathbf{i}}$ is the inlet flow direction, and τ represents the wall shear stress on the surface. The wall shear stress τ can be calculated from the air velocity near the surface, which is typically much smaller than the pressure term. For the drag coefficient of Shape-Net Car, $\hat{\mathbf{i}} = (-1, 0, 0)$ and A is the area of the smallest rectangle enclosing the front of the car. For the lift coefficient of AirFRANS, $\hat{\mathbf{i}} = (0, 0, -1)$. The relative L^2 error is computed between the ground-truth coefficient and the coefficient calculated from the predicted fields.

Spearman’s Rank Correlation. Given K test samples with ground-truth coefficients $C = \{C^1, \dots, C^K\}$ (drag or lift) and model-predicted coefficients $\hat{C} = \{\hat{C}^1, \dots, \hat{C}^K\}$, Spearman’s correlation coefficient is defined as the Pearson correlation coefficient between the rank variables:

$$\rho = \frac{\text{cov}(R(C), R(\hat{C}))}{\sigma_{R(C)} \sigma_{R(\hat{C})}}, \quad (16)$$

where R is the ranking function, cov denotes the covariance, and σ represents the standard deviation of the rank variables. This metric measures the correlation between the ranking distribution of ground-truth coefficients and model-predicted values across all test samples, quantifying the model’s ability to correctly rank different designs. This property is particularly important for shape optimization applications. A Spearman’s correlation close to 1 indicates better performance.

Appendix A.3. Training and Model Configurations

Following the conventions established in prior work (Li et al., 2021; 2023a; Wu et al., 2024; Zhou et al., 2025), our model is trained using the relative L^2 loss. Table 8 summarizes the training configurations shared across all methods for fair comparison, and Table 9 presents PGOT-specific hyperparameters.

Table 8. Training configurations for each benchmark. All methods are trained under identical settings.

Benchmark	Loss	Epochs	Learning Rate	Optimizer	Batch Size
Elasticity	Relative L^2	500	10^{-3}	AdamW	1
Plasticity	Relative L^2	500	10^{-3}	AdamW	8
Airfoil	Relative L^2	500	10^{-3}	AdamW	4
Pipe	Relative L^2	500	10^{-3}	AdamW	4
Shape-Net Car	$\mathcal{L}_v + 0.5\mathcal{L}_s$	200	10^{-3}	Adam	1
AirFRANS	$\mathcal{L}_v + \mathcal{L}_s$	400	10^{-3}	Adam	1

For Shape-Net Car (Umetani & Bickel, 2018) and AirFRANS (Bonnet et al., 2022), \mathcal{L}_v and \mathcal{L}_s denote the relative L^2 losses on volumetric and surface fields.

The hidden dimension C is set to 256 for high-dimensional output tasks (Shape-Net Car and AirFRANS) and 128 for others. Accordingly, the number of latent slices M is adjusted to 32 for $C = 256$ and 64 for $C = 128$ to balance model capacity and computational efficiency. These settings are consistent with the configurations used in Transolver (Wu et al., 2024) and other neural operators, and their effectiveness is further validated by our ablation studies.

Table 9. PGOT model configurations for each benchmark.

Benchmark	Layers L	Channels C	Slices M	Scales S	Heads
Elasticity	8	128	64	2	8
Plasticity	8	128	64	2	8
Airfoil	8	128	64	2	8
Pipe	8	128	64	2	8
Shape-Net Car	8	256	32	3	8
AirfRANS	8	256	32	3	8

Appendix A.4. Baseline Implementations

Neural Operators. For FNO (Li et al., 2021), Geo-FNO (Li et al., 2023a), WMT (Gupta et al., 2021), U-FNO (Wen et al., 2022), U-NO (Rahman et al., 2023), F-FNO (Tran et al., 2023), and LSM (Wu et al., 2023), we report results from the original publications (Wu et al., 2024; Zhou et al., 2025; Li et al., 2021).

Transformer-based Methods. For Galerkin Transformer (Cao, 2021), OFormer (Li et al., 2023c), GNOT (Hao et al., 2023), HT-Net (Liu et al., 2024), FactFormer (Li et al., 2023d), and ONO, we report results from the original publications (Wu et al., 2024; Zhou et al., 2025; Li et al., 2021). For Transolver (Wu et al., 2024) and SAOT (Zhou et al., 2025), we reproduce results based on their official codebases with all hyperparameter configurations kept consistent with PGOT to ensure fair comparison.

Geometric Deep Learning Methods. For MLP, GraphSAGE (Hamilton et al., 2017), PointNet (Qi et al., 2017), Graph U-Net (Gao & Ji, 2019), MeshGraphNet (Pfaff et al., 2021), GNO (Li et al., 2020), GINO (Li et al., 2023b), and 3D-GeoCA (Deng et al., 2024), we report results from the original publications.

Appendix B. Supplementary Results

Appendix B.1. Ablation Results

We provide the complete ablation study results on all six benchmarks in Tables 10, 11, and 12.

 Table 10. Full ablation on the number of latent slices M .

M	Plasticity	Pipe	Airfoil	Elasticity	Car (Vol.)	AirfRANS (Vol.)
8	0.0104	0.0079	0.0194	0.0239	0.0421	0.0077
16	0.0047	0.0071	0.0101	0.0074	0.0394	0.0059
32	0.0025	0.0040	0.0060	0.0081	0.0210	0.0025
64	0.0012	0.0039	0.0046	0.0069	0.0299	0.0055
128	0.0021	0.0051	0.0056	0.0061	0.0322	0.0049
256	0.0134	0.0044	0.0048	0.0079	0.0318	0.0104

 Table 11. Full ablation on the number of geometric scales S .

S	Plasticity	Pipe	Airfoil	Elasticity	Car (Vol.)	AirfRANS (Vol.)
1	0.0104	0.0079	0.0194	0.0239	0.0342	0.0029
2	0.0012	0.0039	0.0046	0.0069	0.0237	0.0031
3	0.0047	0.0071	0.0101	0.0074	0.0210	0.0025
4	0.0021	0.0051	0.0056	0.0079	0.0329	0.0098

Table 12. Full ablation on key components.

Variant	Plasticity	Pipe	Airfoil	Elasticity	Car (Vol.)	AirfRANS (Vol.)
w/o SGA	0.0093	0.0045	0.0104	0.0074	0.0482	0.0081
w/o TDF	0.0134	0.0089	0.0094	0.0231	0.0348	0.0076
Full PGOT	0.0012	0.0039	0.0046	0.0069	0.0210	0.0025

Appendix B.2. Efficiency Analysis

Table 13 compares computational efficiency across different mesh sizes. PGOT maintains competitive efficiency while achieving superior accuracy. Compared to Transolver, PGOT requires slightly more GPU memory (5.37 GB vs. 4.02 GB at $N = 32768$) but achieves substantially better prediction quality. Notably, PGOT exhibits excellent scalability: the running time remains nearly constant (58-60 s/epoch) as mesh size increases from 1024 to 16384, confirming the $\mathcal{O}(N)$ linear complexity of SpecGeo-Attention. In contrast, methods like ONO (Xiao et al., 2024) and OFormer (Li et al., 2023c) show significant time increases with mesh size due to their higher computational complexity. At $N = 32768$, PGOT is $4.2\times$ faster than ONO and $1.6\times$ faster than OFormer (Li et al., 2023c) while achieving notably lower prediction errors.

Table 13. Efficiency comparison of Transformer-based methods across different mesh sizes N . Running time is measured by the time (s) to complete one epoch containing 1000 iterations. Params denotes the number of model parameters (MB).

Model	Params	GPU Memory (GB)						Time (s/epoch)					
		1024	2048	4096	8192	16384	32768	1024	2048	4096	8192	16384	32768
Galerkin (2021)	1.041	0.62	0.66	0.74	0.91	1.45	2.05	26.51	26.50	27.48	37.10	67.52	129.87
OFormer (2023c)	0.884	0.63	0.69	0.80	1.02	1.67	2.44	28.15	30.98	31.11	47.90	91.67	182.21
ONO (2024)	1.109	1.47	1.75	2.30	3.47	5.64	10.09	69.76	76.25	100.13	149.59	255.34	462.46
GNOT (2023)	5.248	0.85	1.07	1.47	2.33	4.23	7.46	54.28	55.94	60.86	67.17	112.55	209.92
Transolver (2024)	0.950	0.15	0.27	0.53	1.02	2.03	4.02	38.43	38.56	37.33	38.36	51.73	98.54
SAOT (2025)	1.492	0.33	0.52	0.92	1.61	3.11	6.33	94.09	94.72	97.01	97.22	132.33	234.94
PGOT (Ours)	1.148	0.20	0.37	0.71	1.38	2.71	5.37	58.04	59.76	59.52	60.44	60.17	110.99

Appendix B.3. Out-of-Distribution Generalization

We evaluate PGOT under two extrapolation settings on AirfRANS: (1) Unseen Reynolds numbers and (2) Unseen angles of attack. The detailed experimental settings are provided in Table 14, where the training and test sets contain completely different Reynolds numbers or angles of attack.

Table 14. Settings of OOD generalization experiments on AirfRANS. The range of Reynolds numbers and angles of attack are listed.

Dataset	Unseen Reynolds		Unseen Angles	
	Reynolds Range	Samples	Angles Range	Samples
Training Set	$[3 \times 10^6, 5 \times 10^6]$	500	$[-2.5, 12.5]$	800
Test Set	$[2 \times 10^6, 3 \times 10^6] \cup [5 \times 10^6, 6 \times 10^6]$	500	$[-5, -2.5] \cup [12.5, 15]$	200

Table 15 presents the comprehensive evaluation of 12 models on AirfRANS extrapolation tasks. Beyond the Lift Coefficient (C_L) and its ranking correlation (ρ_L) reported in the main text, we additionally provide the Mean Squared Error (MSE) for surrounding (Volume) and surface (Surf) physics fields to offer a holistic view of model robustness.

Performance Analysis. Graph-based methods (e.g., MeshGraphNet (Pfaff et al., 2021), Graph U-Net (Gao & Ji, 2019)) exhibit significant degradation in extrapolation settings. For instance, MeshGraphNet incurs a relative error of 1.7718 for C_L in Reynolds extrapolation. Fundamentally, these Message Passing Neural Networks tend to overfit the local connectivity statistics of the training mesh. When the Reynolds number increases, the physical boundary layer thins, introducing sharp gradients that alter the effective physical length scales; Message Passing Neural Networks, constrained by learned local receptive fields, fail to adapt to this shift. While Transformer-based baselines like Transolver (Wu et al., 2024) and SAOT (Zhou et al., 2025) improve upon this by leveraging global attention, they still rely heavily on latent feature similarity

Table 15. Full OOD generalization results on AirfRANS. PGOT achieves the best overall performance, particularly in ranking consistency (ρ_L) and field reconstruction (Volume/Surf). Best results are **bolded**, second best are underlined.

Model	Unseen Reynolds Numbers				Unseen Angles of Attack			
	Volume ↓	Surf ↓	C_L ↓	ρ_L ↑	Volume ↓	Surf ↓	C_L ↓	ρ_L ↑
Simple MLP	0.0669	0.1153	0.6205	0.9578	0.1309	0.3311	0.4128	0.9572
GraphSAGE (2017)	0.0798	0.1254	0.4333	0.9707	0.1192	0.2359	0.2538	0.9894
PointNet (2017)	0.0838	0.1403	0.3836	0.9806	0.2021	0.4649	0.4425	0.9784
Graph U-Net (2019)	0.0538	0.1168	0.4664	0.9645	0.0979	0.2391	0.3756	0.9816
MeshGraphNet (2021)	0.2789	0.2382	1.7718	0.7631	0.4902	1.1071	0.6525	0.8927
GNO (2020)	0.0833	0.1562	0.4408	0.9878	0.1626	0.2359	0.3038	0.9884
Galerkin (2021)	0.0330	0.0972	0.4615	0.9826	0.0577	0.2773	0.3814	0.9821
GNOT (2023)	0.0305	0.0959	0.3268	0.9865	0.0471	0.3466	0.3497	0.9868
GINO (2023b)	0.0839	0.1825	0.4180	0.9645	0.1589	0.2469	0.2583	0.9923
Transolver (2024)	<u>0.0234</u>	<u>0.0341</u>	<u>0.3042</u>	0.9899	<u>0.0454</u>	<u>0.2279</u>	0.1503	0.9948
SAOT (2025)	0.1032	0.1193	0.4242	0.9764	0.0748	0.2744	0.2925	0.9888
PGOT (Ours)	0.0203	0.0293	0.2942	0.9923	0.0348	0.2203	<u>0.1742</u>	0.9952

for token clustering. In scenarios with severe flow separation, the feature distribution shifts drastically, leading to unstable slicing and degraded field reconstruction.

In contrast, PGOT achieves strong stability across most metrics, obtaining the best performance in 7 out of 8 evaluation criteria. While Transolver slightly outperforms PGOT on C_L in the Unseen Angles setting (0.1503 vs. 0.1742), PGOT achieves superior ranking correlation (ρ_L : 0.9952 vs. 0.9948), which is more critical for design optimization as it measures the model’s ability to correctly rank different airfoil designs. Moreover, PGOT consistently achieves the lowest field reconstruction errors (Volume and Surf) in both OOD settings, demonstrating that its geometric anchoring mechanism provides more reliable physical field predictions even when the coefficient prediction is slightly less accurate.

Appendix C. Additional Visualizations

Appendix C.1. Learned Slice Assignments of SpecGeo-Attention

Figures 6–11 visualize the learned slice assignments from SpecGeo-Attention across all six benchmarks. Each subplot represents one of 32 latent physical states, where different colors indicate varying assignment intensities.

Appendix C.2. Gate Activations of TaylorDecomp-FFN

Figures 12–17 visualize the gate activations $\alpha(g)$ from TaylorDecomp-FFN. Each subplot displays the gate values for one of 64 feature channels. Red indicates high activation (routing to the non-linear expert) and blue indicates low activation (routing to the linear expert).

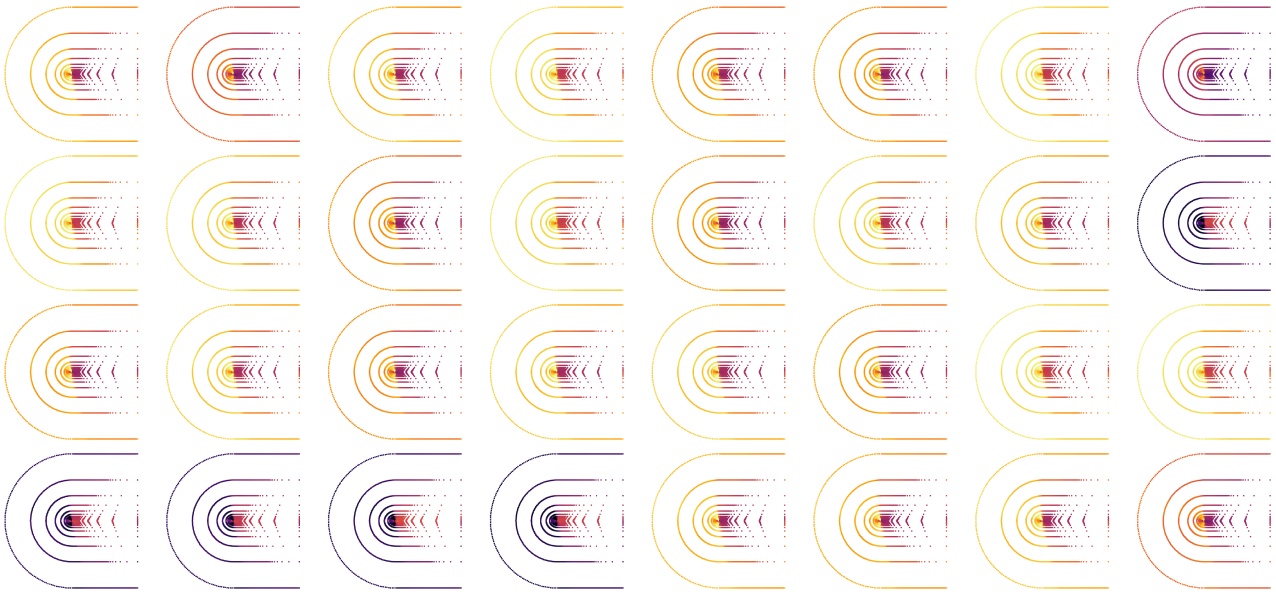


Figure 6. Learned slice assignments from SpecGeo-Attention on Airfoil (32 slices).



Figure 7. Learned slice assignments from SpecGeo-Attention on Pipe (32 slices).

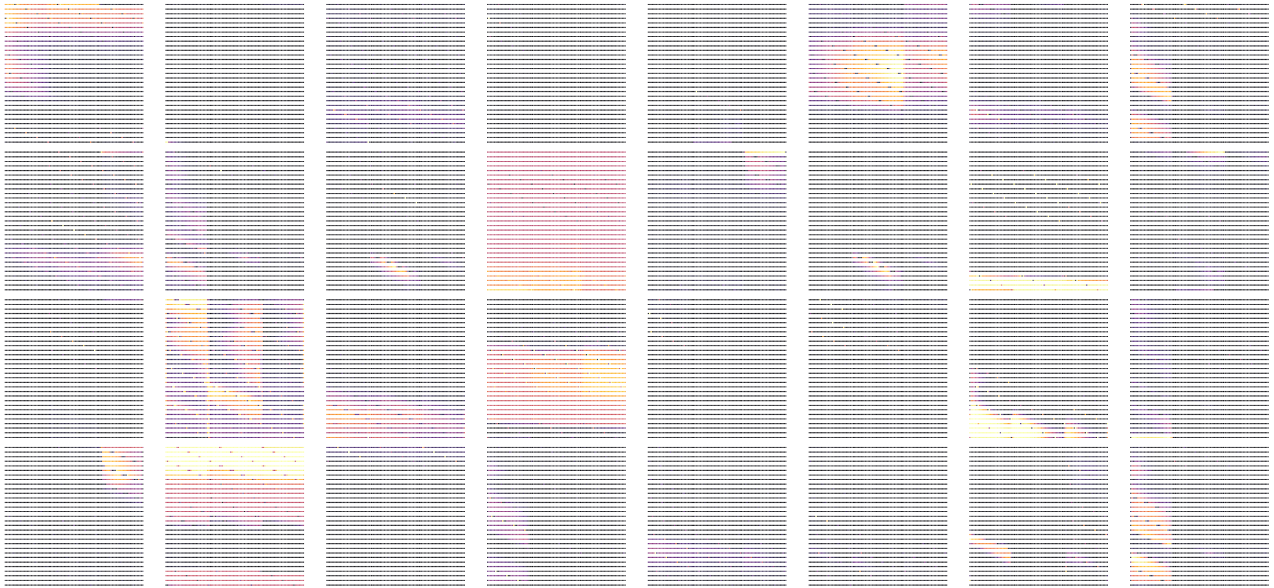


Figure 8. Learned slice assignments from SpecGeo-Attention on Plasticity (32 slices).

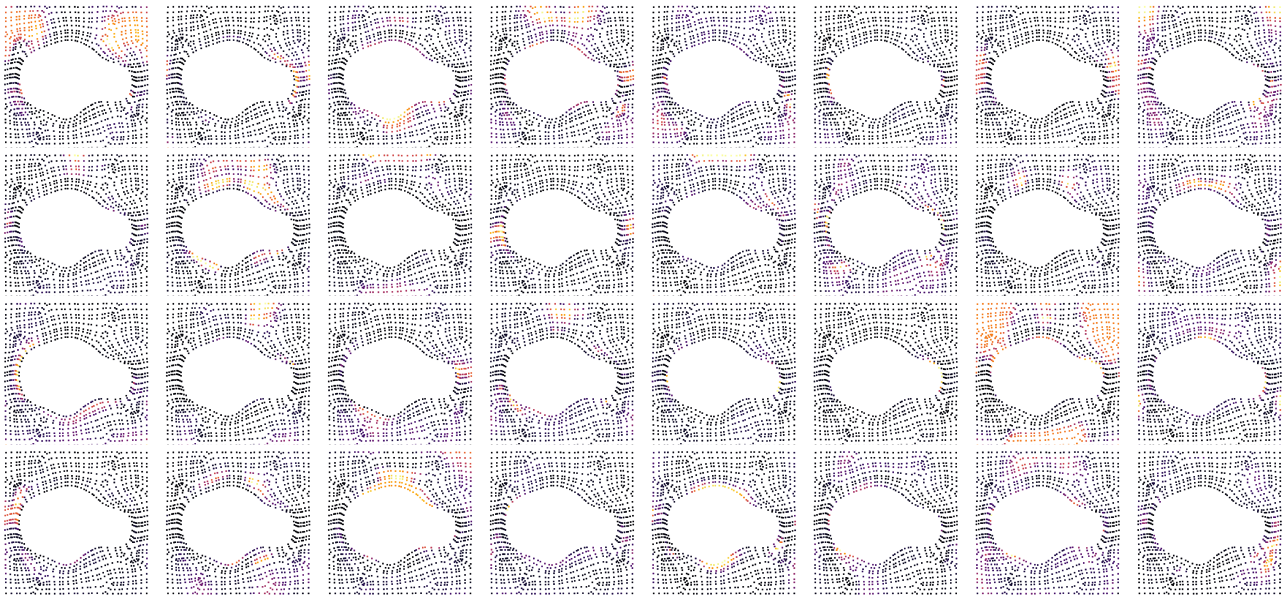


Figure 9. Learned slice assignments from SpecGeo-Attention on Elasticity (32 slices).

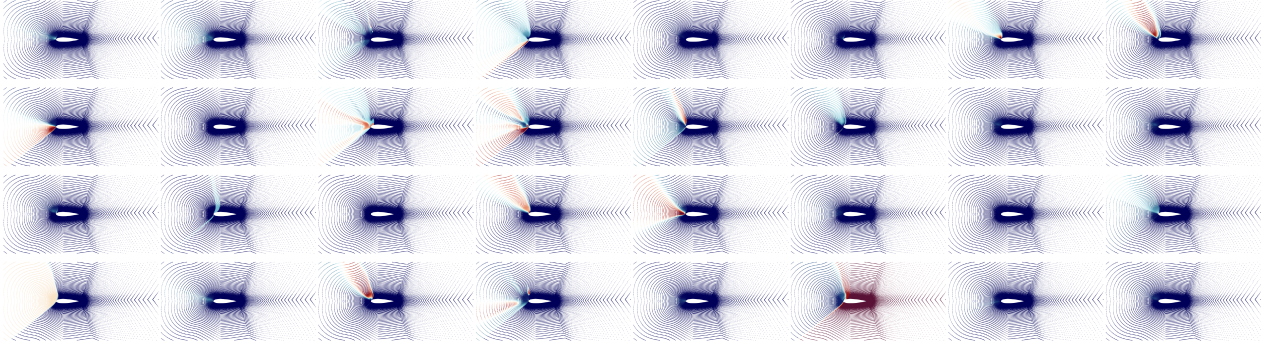


Figure 10. Learned slice assignments from SpecGeo-Attention on AirfRANS (32 slices).

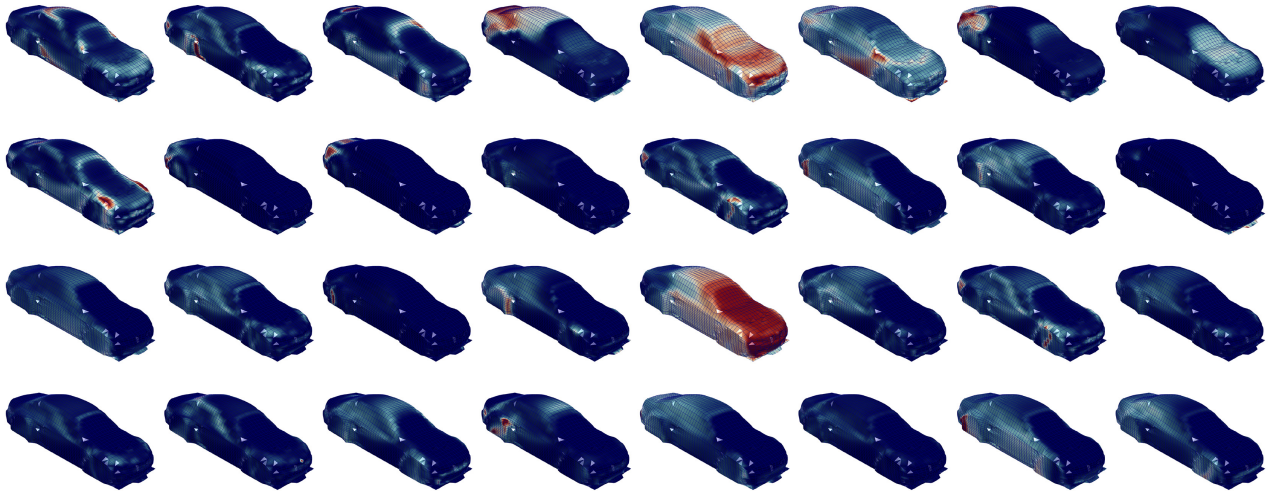


Figure 11. Learned slice assignments from SpecGeo-Attention on Shape-Net Car (32 slices).

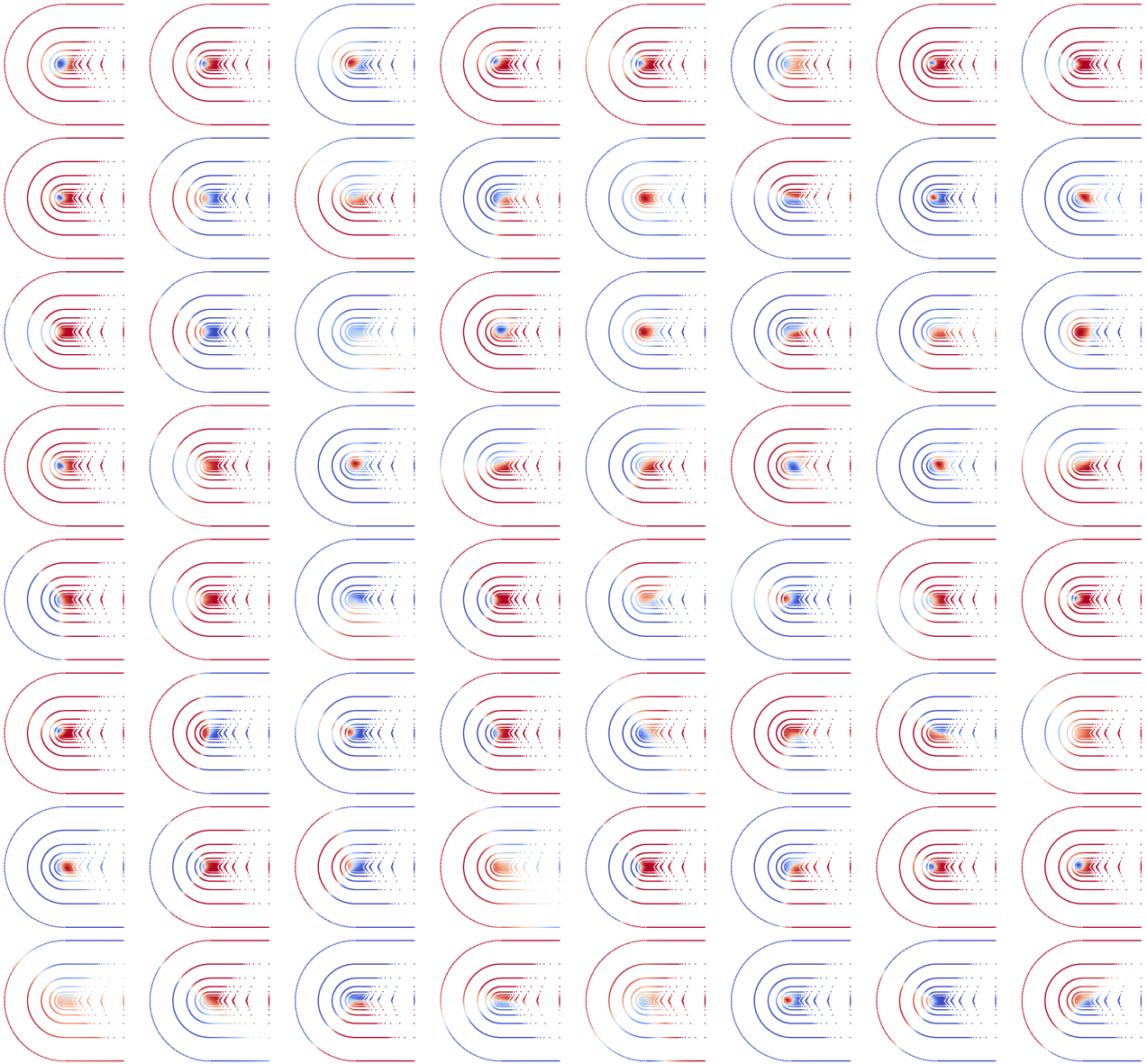


Figure 12. Gate activations from TaylorDecomp-FFN on Airfoil (64 channels).

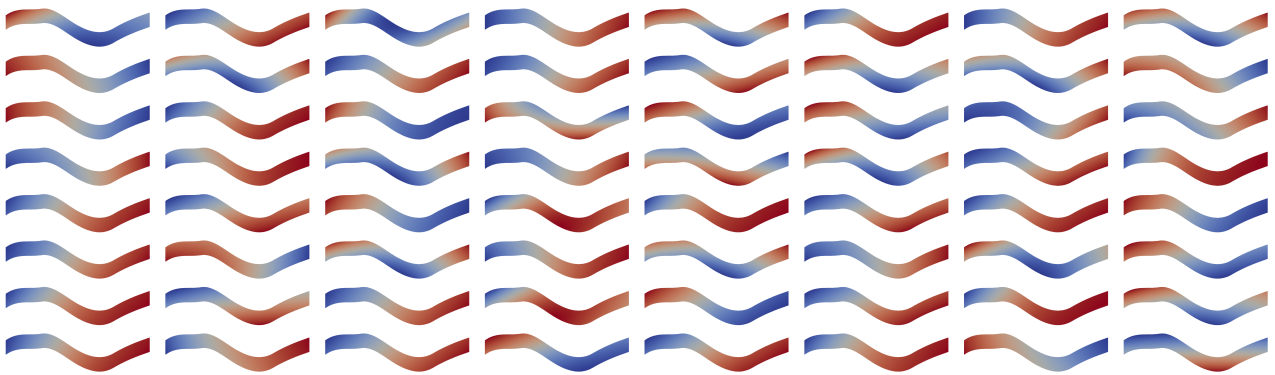


Figure 13. Gate activations from TaylorDecomp-FFN on Pipe (64 channels).

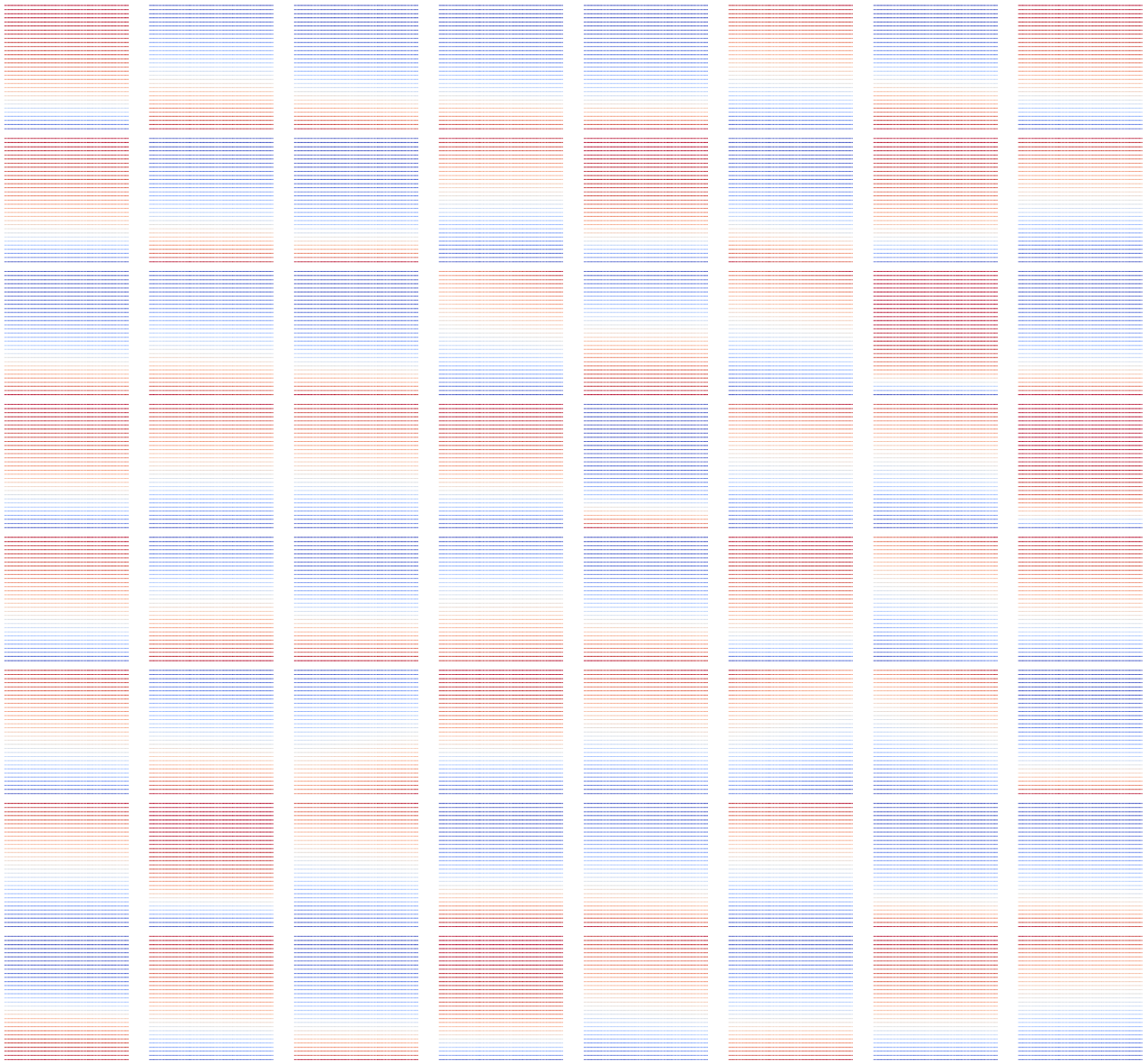


Figure 14. Gate activations from TaylorDecomp-FFN on Plasticity (64 channels).

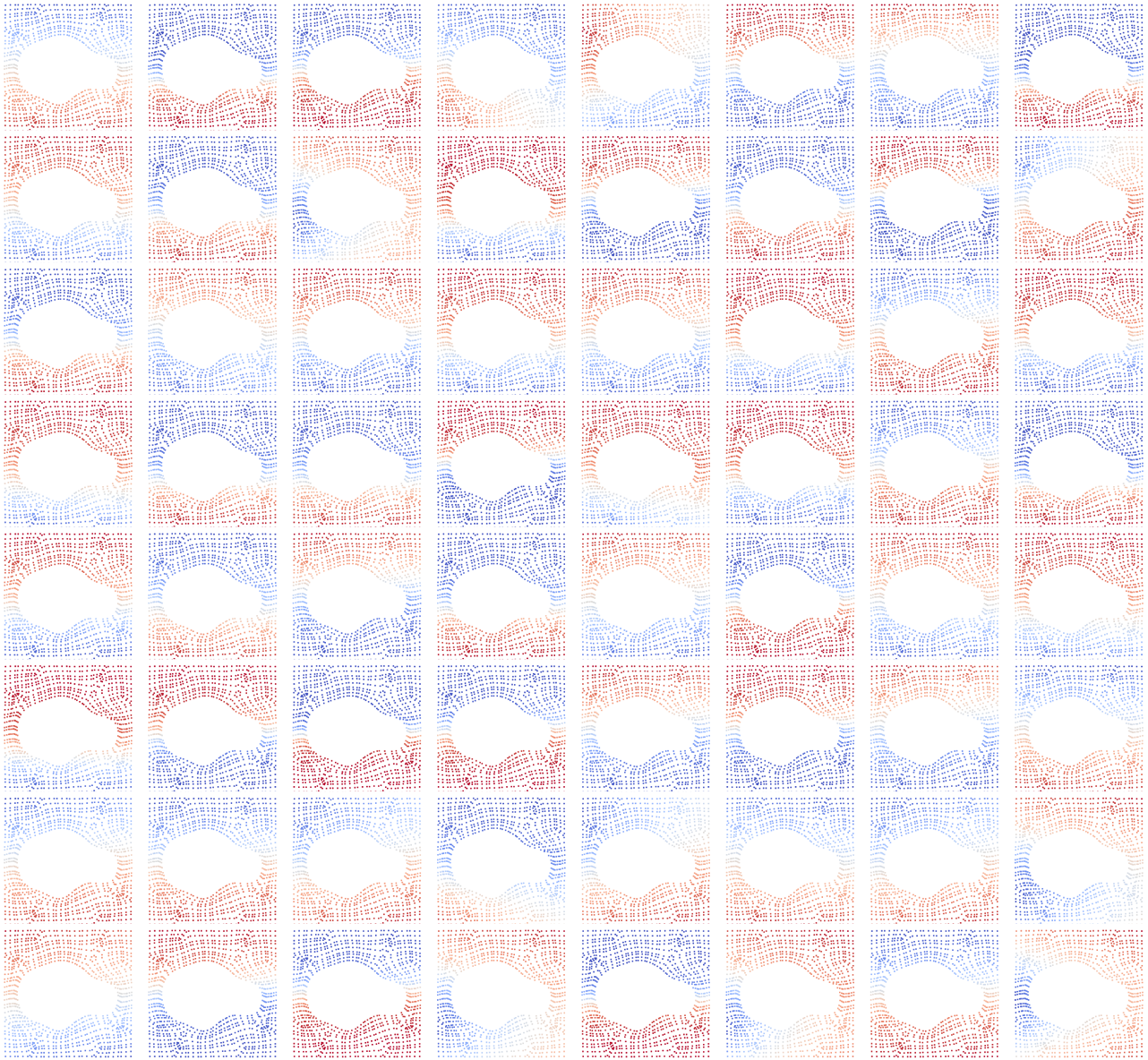


Figure 15. Gate activations from TaylorDecomp-FFN on Elasticity (64 channels).

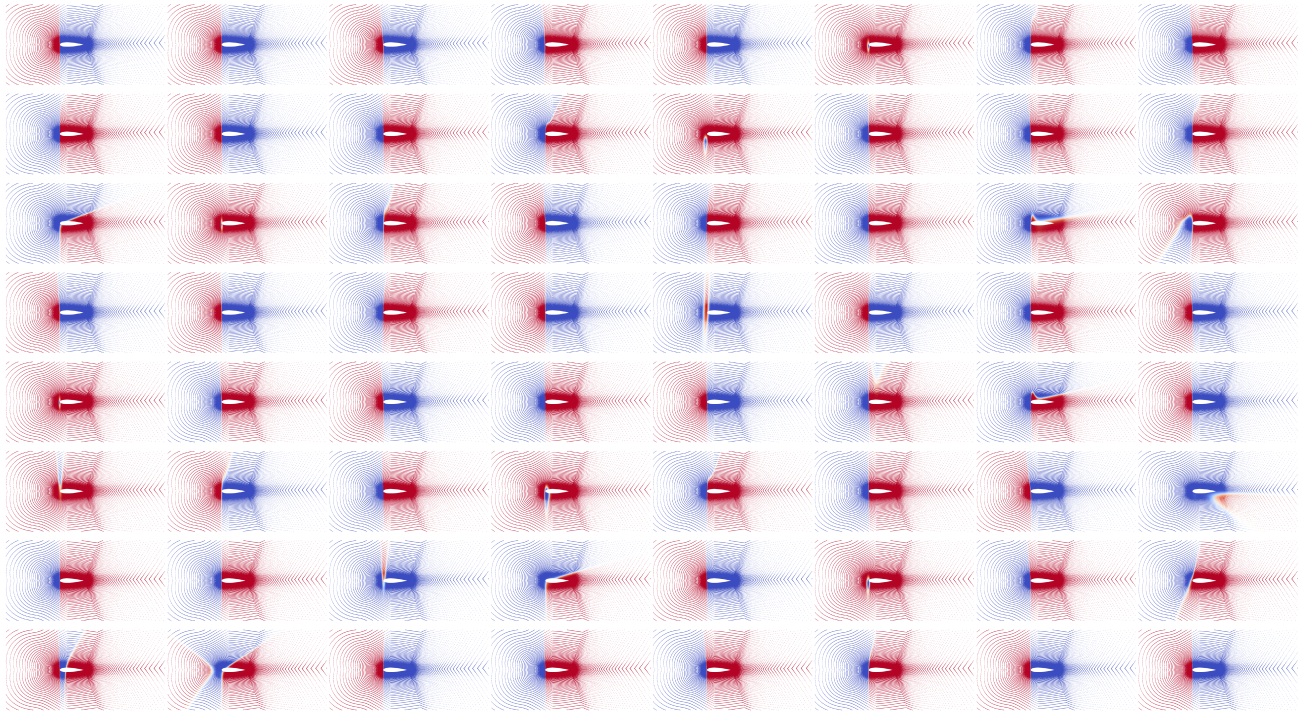


Figure 16. Gate activations from TaylorDecomp-FFN on AirfRANS (64 channels).

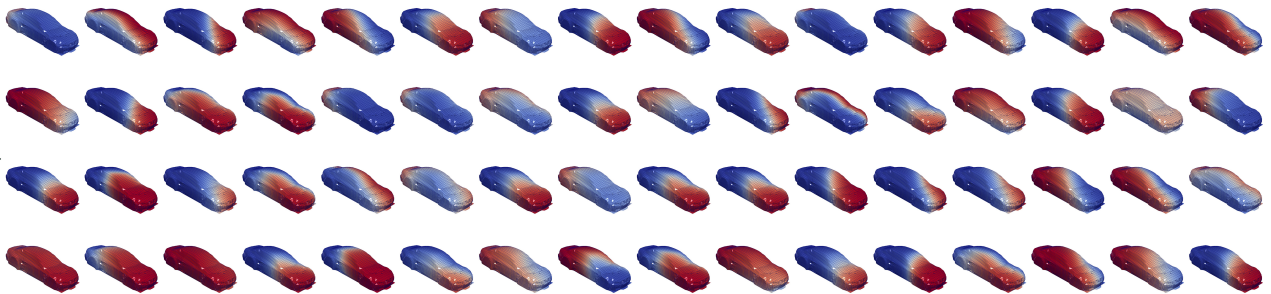


Figure 17. Gate activations from TaylorDecomp-FFN on Shape-Net Car (64 channels).

References

- Alkin, B., Fürst, A., Schmid, S., Gruber, L., Holzleitner, M., and Brandstetter, J. Universal physics transformers: A framework for efficiently scaling neural operators. In *NeurIPS 2024, Vancouver, BC, Canada, December 10 - 15, 2024*, 2024.
- Bonnet, F., Mazari, J., Cinnella, P., and Gallinari, P. Airfrans: High fidelity computational fluid dynamics dataset for approximating reynolds-averaged navier–stokes solutions. *Advances in Neural Information Processing Systems*, 35: 23463–23478, 2022.
- Cao, S. Choose a transformer: Fourier or galerkin. In *NeurIPS 2021, December 6-14, 2021, virtual*, pp. 24924–24940, 2021.
- Cao, W., Shan, X., Tang, S., Ouyang, W., and Zhang, W. Solving parametric high-reynolds-number wall-bounded turbulence around airfoils governed by reynolds-averaged navier–stokes equations using time-stepping-oriented neural network. *Physics of Fluids*, 37(1), 2025.
- Chen, X. et al. Gnnrl-smoothing: A prior-free reinforcement learning model for mesh optimization. *Neural Networks*, pp. 108235, 2025.
- Cheng, S. and Alkhalifah, T. Meta learning for improved neural network wavefield solutions. *Surveys in Geophysics*, 46(1): 145–167, 2025.
- Cho, W., Jo, M., Lim, H., Lee, K., Lee, D., Hong, S., and Park, N. Parameterized physics-informed neural networks for parameterized pdes. In *ICML 2024, Vienna, Austria, July 21-27, 2024*. OpenReview.net, 2024.
- Deng, J., Li, X., Xiong, H., Hu, X., and Ma, J. Geometry-guided conditional adaptation for surrogate models of large-scale 3d pdes on arbitrary geometries. In *IJCAI 2024, Jeju, South Korea, August 3-9, 2024*, pp. 5790–5798. ijcai.org, 2024.
- Eymard, R., Gallouët, T., and Herbin, R. Finite volume methods. *Handbook of Numerical Analysis*, 7:713–1018, 2000.
- Gao, H. and Ji, S. Graph u-nets. In *International Conference on Machine Learning*, pp. 2083–2092. PMLR, 2019.
- Guibas, J., Mardani, M., Li, Z., Tao, A., Anandkumar, A., and Catanzaro, B. Efficient token mixing for transformers via adaptive fourier neural operators. In *ICLR 2022, Virtual Event, April 25-29, 2022*. OpenReview.net, 2022.
- Gupta, G., Xiao, X., and Bogdan, P. Multiwavelet-based operator learning for differential equations. In *NeurIPS 2021, December 6-14, 2021, virtual*, pp. 24048–24062, 2021.
- Hamilton, W., Ying, Z., and Leskovec, J. Inductive representation learning on large graphs. *Advances in Neural Information Processing Systems*, 30, 2017.
- Hao, Z., Wang, Z., Su, H., Ying, C., Dong, Y., Liu, S., Cheng, Z., Song, J., and Zhu, J. GNOT: A general neural operator transformer for operator learning. In *ICML 2023, 23-29 July 2023, Honolulu, Hawaii, USA*, volume 202 of *Proceedings of Machine Learning Research*, pp. 12556–12569. PMLR, 2023.
- Koshizuka, T., Fujisawa, M., Tanaka, Y., and Sato, I. Understanding the expressivity and trainability of fourier neural operator: A mean-field perspective. In *NeurIPS 2024, Vancouver, BC, Canada, December 10 - 15, 2024*, 2024.
- Kovachki, N., Li, Z., Liu, B., Azzadenesheli, K., Bhattacharya, K., Stuart, A., and Anandkumar, A. Neural operator: Learning maps between function spaces with applications to pdes. *Journal of Machine Learning Research*, 24(89):1–97, 2023.
- Lee, S. and Oh, T. Inducing point operator transformer: A flexible and scalable architecture for solving pdes. In *Proceedings of the AAAI Conference on Artificial Intelligence*, volume 38, pp. 153–161, 2024.
- Lee-Thorp, J., Ainslie, J., Eckstein, I., and Ontañón, S. Fnet: Mixing tokens with fourier transforms. In *NAACL 2022, Seattle, WA, United States, July 10-15, 2022*, pp. 4296–4313. Association for Computational Linguistics, 2022.
- Li, S., Yoo, S., and Yang, Y. Maximal update parametrization and zero-shot hyperparameter transfer for fourier neural operators. In *ICML 2025, Vancouver, BC, Canada, July 13-19, 2025*. OpenReview.net, 2025.

- Li, Z., Kovachki, N., Azizzadenesheli, K., Liu, B., Bhattacharya, K., Stuart, A., and Anandkumar, A. Neural operator: Graph kernel network for partial differential equations. *arXiv preprint arXiv:2003.03485*, 2020.
- Li, Z., Kovachki, N. B., Azizzadenesheli, K., Liu, B., Bhattacharya, K., Stuart, A. M., and Anandkumar, A. Fourier neural operator for parametric partial differential equations. In *ICLR 2021, Virtual Event, Austria, May 3-7, 2021*. OpenReview.net, 2021.
- Li, Z., Huang, D. Z., Liu, B., and Anandkumar, A. Fourier neural operator with learned deformations for pdes on general geometries. *Journal of Machine Learning Research*, 24(388):1–26, 2023a.
- Li, Z., Kovachki, N. B., Choy, C. B., Li, B., Kossaifi, J., Otta, S. P., Nabian, M. A., Stadler, M., Hundt, C., Azizzadenesheli, K., and Anandkumar, A. Geometry-informed neural operator for large-scale 3d pdes. In *NeurIPS 2023, New Orleans, LA, USA, December 10 - 16, 2023*, 2023b.
- Li, Z., Meidani, K., and Farimani, A. B. Transformer for partial differential equations’ operator learning. *Transactions on Machine Learning Research*, 2023c.
- Li, Z., Shu, D., and Farimani, A. B. Scalable transformer for PDE surrogate modeling. In *NeurIPS 2023, New Orleans, LA, USA, December 10 - 16, 2023*, 2023d.
- Liu, X., Xu, B., Cao, S., and Zhang, L. Mitigating spectral bias for the multiscale operator learning. *Journal of Computational Physics*, 506:112944, 2024.
- Lu, L., Jin, P., Pang, G., Zhang, Z., and Karniadakis, G. E. Learning nonlinear operators via deeponet based on the universal approximation theorem of operators. *Nature Machine Intelligence*, 3(3):218–229, 2021.
- Luo, H., Wu, H., Zhou, H., Xing, L., Di, Y., Wang, J., and Long, M. Transolver++: An accurate neural solver for pdes on million-scale geometries. In *ICML 2025, Vancouver, BC, Canada, July 13-19, 2025*. OpenReview.net, 2025.
- Morris, E., Shen, H., Du, W., Sajjad, M. H., and Shi, B. Geometric instability of graph neural networks on large graphs. *arXiv preprint arXiv:2308.10099*, 2023.
- Pfaff, T., Fortunato, M., Sanchez-Gonzalez, A., and Battaglia, P. W. Learning mesh-based simulation with graph networks. In *ICLR 2021, Virtual Event, Austria, May 3-7, 2021*. OpenReview.net, 2021.
- Qi, C. R., Su, H., Mo, K., and Guibas, L. J. Pointnet: Deep learning on point sets for 3d classification and segmentation. In *Proceedings of the IEEE Conference on Computer Vision and Pattern Recognition*, pp. 652–660, 2017.
- Rahman, M. A., Ross, Z. E., and Azizzadenesheli, K. U-NO: u-shaped neural operators. *Transactions on Machine Learning Research*, 2023, 2023.
- Raissi, M., Perdikaris, P., and Karniadakis, G. E. Physics-informed neural networks: A deep learning framework for solving forward and inverse problems involving nonlinear partial differential equations. *Journal of Computational physics*, 378: 686–707, 2019.
- Rao, Y., Zhao, W., Zhu, Z., Lu, J., and Zhou, J. Global filter networks for image classification. In *NeurIPS 2021, December 6-14, 2021, virtual*, pp. 980–993, 2021.
- Tran, A., Mathews, A. P., Xie, L., and Ong, C. S. Factorized fourier neural operators. In *ICLR 2023, Kigali, Rwanda, May 1-5, 2023*. OpenReview.net, 2023.
- Tripura, T. and Chakraborty, S. Wavelet neural operator for solving parametric partial differential equations in computational mechanics problems. *Computer Methods in Applied Mechanics and Engineering*, 404:115783, 2023.
- Umetani, N. and Bickel, B. Learning three-dimensional flow for interactive aerodynamic design. *ACM Transactions on Graphics (TOG)*, 37(4):1–10, 2018.
- Vaswani, A., Shazeer, N., Parmar, N., Uszkoreit, J., Jones, L., Gomez, A. N., Kaiser, Ł., and Polosukhin, I. Attention is all you need. *Advances in Neural Information Processing Systems*, 30, 2017.

- Wang, R., Xia, Z., Yan, G., and Yan, J. Quanonet: Quantum neural operator with application to differential equation. In *ICML 2025, Vancouver, BC, Canada, July 13-19, 2025*. OpenReview.net, 2025a.
- Wang, T. and Wang, C. Latent neural operator for solving forward and inverse PDE problems. In *NeurIPS 2024, Vancouver, BC, Canada, December 10 - 15, 2024*, 2024.
- Wang, Y., Bai, J., Eshaghi, M. S., Anitescu, C., Zhuang, X., Rabczuk, T., and Liu, Y. Transfer learning in physics-informed neurals networks: Full fine-tuning, lightweight fine-tuning, and low-rank adaptation. *International Journal of Mechanical System Dynamics*, 2025b.
- Wen, G., Li, Z., Azizzadenesheli, K., Anandkumar, A., and Benson, S. M. U-fno—an enhanced fourier neural operator-based deep-learning model for multiphase flow. *Advances in Water Resources*, 163:104180, 2022.
- Wu, H., Hu, T., Luo, H., Wang, J., and Long, M. Solving high-dimensional pdes with latent spectral models. In *ICML 2023, 23-29 July 2023, Honolulu, Hawaii, USA*, volume 202 of *Proceedings of Machine Learning Research*, pp. 37417–37438. PMLR, 2023.
- Wu, H., Luo, H., Wang, H., Wang, J., and Long, M. Transolver: A fast transformer solver for pdes on general geometries. In *ICML 2024, Vienna, Austria, July 21-27, 2024*. OpenReview.net, 2024.
- Xiao, Z., Hao, Z., Lin, B., Deng, Z., and Su, H. Improved operator learning by orthogonal attention. In *ICML 2024, Vienna, Austria, July 21-27, 2024*. OpenReview.net, 2024.
- Zhang, S., Zhong, Y., Yang, X., Wang, W., Zhang, Z., Guo, X.-W., and Yang, C. Discrete-time physics-informed neural networks for two-phase flow interface capturing. In *Proceedings of the 8th International Conference on Computer Science and Application Engineering*, pp. 24–30, 2024.
- Zhang, Z., Xiong, X., Zhang, S., Wang, W., Yang, X., Zhang, S., and Yang, C. A pseudo-time stepping and parameterized physics-informed neural network framework for navier stokes equations. *Physics of Fluids*, 37(3), 2025a.
- Zhang, Z., Xiong, X., Zhang, S., Wang, W., Zhong, Y., Yang, C., and Yang, X. Legend-kinn: A legendre polynomial-based kolmogorov-arnold-informed neural network for efficient pde solving. *Expert Systems with Applications*, pp. 129839, 2025b.
- Zhou, C., Chen, J., and Yang, Z. Saot: An enhanced locality-aware spectral transformer for solving pdes. In *AAAI*, 2025.
- Zienkiewicz, O. C. and Taylor, R. L. *The Finite Element Method Set*. Elsevier, 2005.